The Astrophysical Journal Letters, 926:L25 (8pp), 2022 February 20 https://doi.org/10.3847/2041-8213/ac4fbd

A Rapid Ionization Change in the Nebular-phase Spectra of the Type Ia SN 2011fe

M. A. Tucker[1,5], C. Ashall[1], B. J. Shappee[1], C. S. Kochanek[2,3], K. Z. Stanek[2,3], and P. Garnavich[4]
[1] Institute for Astronomy, University of Hawai'i at Manoa, 2680 Woodlawn Drive, Honolulu, HI, USA; tuckerma95@gmail.com
[2] Department of Astronomy, The Ohio State University, 140 West 18th Avenue, Columbus, OH 43210, USA
[3] Center for Cosmology and AstroParticle Physics, The Ohio State University, 191 W. Woodruff Avenue, Columbus, OH 43210, USA
[4] Physics Department, University of Notre Dame, Notre Dame, IN 46556, USA
Received 2021 October 29; revised 2022 January 11; accepted 2022 January 18; published 2022 February 21

Abstract

We present three new spectra of the nearby Type Ia supernova (SN Ia) 2011fe covering ≈480–850 days after maximum light and show that the ejecta undergoes a rapid ionization shift at ∼500 days after explosion. The prominent Fe III emission lines at ≈4600 Å are replaced with Fe I+Fe II blends at ∼4400 Å and ∼5400 Å. The ≈7300 Å feature, which is produced by [Fe II]+[Ni II] at $\lesssim$400 days after explosion, is replaced by broad (≈±15,000 km s^{-1}) symmetric [Ca II] emission. Models predict this ionization transition occurring ∼100 days later than what is observed, which we attribute to clumping in the ejecta. Finally, we use the nebular-phase spectra to test several proposed progenitor scenarios for SN 2011fe. Nondetections of H and He exclude nearby nondegenerate companions, [O I] nondetections disfavor the violent merger of two white dwarfs, and the symmetric emission-line profiles favor a symmetric explosion.

Unified Astronomy Thesaurus concepts: Type Ia supernovae (1728); Supernovae (1668); White dwarf stars (1799)

Supporting material: data behind figures

1. Introduction

Type Ia supernovae (SNe Ia) are the thermonuclear explosions of carbon/oxygen (C/O) white dwarfs (WDs; Hoyle & Fowler 1960) and produce the majority of iron-group elements in the universe (e.g., Iwamoto et al. 1999). These stellar explosions attracted much attention due their use as standardizable candles (Phillips 1993), but we still lack a genuine understanding of how and why some WDs explode as SNe Ia.

SN 2011fe was discovered ≈11 hr after explosion by the Palomar Transient Facility (PTF; Law et al. 2009) in M101 at a mere 6.4 Mpc (e.g., Shappee & Stanek 2011) and became the brightest SN Ia in several decades. Additionally, SN 2011fe is the quintessential SN Ia (Pereira et al. 2013), making it an ideal object for testing SN Ia progenitor and explosion models (e.g., Röpke et al. 2012). This is especially important for nebular-phase observations when the ejecta becomes optically thin to optical and NIR photons to provide a direct view to the inner ejecta.

Several studies have already analyzed spectra of SN 2011fe as it transitioned into the nebular phase. Shappee et al. (2013) and Lundqvist et al. (2015) searched for Hα emission indicative of a nearby donor star at the time of explosion and found none. McClelland et al. (2013) showed that the nebular-phase mid-infrared (MIR) decay is correlated with the nucleosynthetic yield. Mazzali et al. (2015) modeled a suite of photospheric- and nebular-phase spectra and claimed the existence of a stable iron core, although this remains debated (e.g., Botyánszki & Kasen 2017). Finally, Taubenberger et al. (2015) and Graham et al. (2015a) analyzed spectra acquired ≈1000 days after maximum light, the latest spectra of an SN Ia to date. They found that the emission characteristics were drastically different from the previous spectra at ≈300 days. Models by Fransson & Jerkstrand (2015) show that the 1000 day spectrum is dominated by Fe I emission lines with minor contributions from Fe II and Ca. However, the spectroscopic evolution between ∼400–1000 days after explosion remains poorly understood. Friesen et al. (2017) briefly attempted to model the +576 days spectrum from Graham et al. (2015a) obtained by the Berkeley SuperNova Identification Program (BSNIP; Silverman et al. 2012), but the results were unsatisfactory and they focused on modeling earlier-phase spectra.

In this Letter we analyze new nebular-phase spectra of SN 2011fe acquired ≈480–850 days after peak light. Details about the data reduction and calibration are provided in Section 2. Section 3 presents the temporal evolution including a distinct change in the iron blends at 4000–6000 Å and the appearance of [Ca II]. Constraints on the progenitor system and explosion mechanism are described in Section 4. Finally, we discuss the rapid ionization change in the context of SN Ia models and the use of [Ca II] as an ejecta diagnostic in Section 5. For our analysis we adopt the time of maximum light in the B band of t_{max} = MJD 55813.98 ± 0.03 from Zhang et al. (2016). This is interchangeable with the time of explosion using the ≈18 day rise time of SN 2011fe from Pereira et al. (2013). We use the distance to M101 of 6.4 Mpc (Shappee & Stanek 2011) as in previous studies, and all phases are given relative to t_{max} in the SN rest frame.

2. New and Archival Spectra

We obtained new spectroscopic observations of SN 2011fe ≈480–850 days after maximum light with the Multi-Object Double Spectrograph (MODS; Pogge et al. 2010) on the Large Binocular Telescope (LBT). Details about the spectroscopic data reduction are described in Shappee et al. (2013). In brief, each frame is bias-subtracted and flat-fielded before detecting and removing cosmic rays with LACOSMIC (van Dokkum 2001). Then, we extract the 1D spectrum with IRAF and derive

[5] DOE CSGF Fellow.

Table 1
New LBT MODS Spectroscopy

UT Date	Phase[a] [days]	Exp. Time [s]
2013-01-05	482.6	14650
2013-05-01	598.4	10800
2014-01-06	848.2	10800

Note.
[a] Relative to t_{max}.

the wavelength calibration with arc-lamp frames. Finally, each spectrum is corrected for instrumental response and placed on a *relative* flux scale with standard star observations. Table 1 summarizes the observations.

Archival spectra from Shappee et al. (2013), Graham et al. (2015b), Graham et al. (2015a), Taubenberger et al. (2015), Mazzali et al. (2015), and Zhang et al. (2016) are included in our analysis to increase the temporal coverage. We also use photometric observations from Munari et al. (2013), Tsvetkov et al. (2013), Zhang et al. (2016), and Shappee et al. (2017) to place the spectra on an absolute flux scale. We restrict the photometry to the *BVR* filters because (1) our spectral analysis is focused on the wavelength range covered by these filters, and (2) data from these filters are available for the spectral epochs used in our analysis (e.g., Figure 1 from Tucker et al. 2021a). We fit the light curves with low-order splines over the range of 200–1000 days. We added Gaussian deviates of the estimated noise and refit the data multiple times to estimate the uncertainties in the spline model. To account for minor differences in the filter throughputs between the photometric setups we include a conservative 0.05 mag (∼5%) systematic uncertainty in the final spline fit.

To flux-calibrate each spectrum, we interpolate the *BVR* magnitudes and uncertainties using the spline fits. The synthetic *BVR* filter magnitude is calculated from the spectrum using Equation (7) from Fukugita et al. (1996), and the spectrum is linearly scaled to match the observed *BVR* magnitudes. Nebular-phase photometry in other optical filters (*gri*; Kerzendorf et al. 2014; Firth et al. 2015; Kerzendorf et al. 2017) is used to check that the spectroscopic flux calibration is correct given the measurement uncertainties.

3. Temporal Evolution

Line identification at $\lesssim$300 days after maximum light is well established due to the increasing number of nebular spectra obtained in recent years (e.g., Graham et al. 2017; Maguire et al. 2018; Sand et al. 2018; Tucker et al. 2020) and improvements in modeling these phases (e.g., Mazzali et al. 2015; Flörs et al. 2018; Wilk et al. 2018; Flörs et al. 2020; Shingles et al. 2020; Wilk et al. 2020; Polin et al. 2021). Optical spectra ∼200–300 days after t_{max} are dominated by Fe III with contributions from [Fe II], [Ni II], and [Co 3]. Figure 1 shows the flux-calibrated spectral evolution at >200 days after t_{max}, and Figure 2 shows the normalized spectra at various epochs. We discuss the evolution of the 4000–6000 Å and ≈7300 Å regions in Sections 3.1 and 3.2, respectively.

3.1. The Fe-dominated 4000–6000 Å Region

The 4000–6000 Å wavelength range is mainly composed of forbidden iron emission lines (e.g., Mazzali et al. 2015; Wilk et al. 2020). The strongest feature in nebular spectra is typically the peak at ∼4600 Å observed in almost all nebular SNe Ia spectra and attributed to a blend of Fe III transitions (e.g., Graham et al. 2017; Maguire et al. 2018; Tucker et al. 2020). Figures 1 and 2 show that this feature dominates the spectrum until ∼400 days after t_{max}. It then disappears over the subsequent 200 days leaving two adjacent peaks at ∼4400 Åand ∼5300 Å. Fransson & Jerkstrand (2015) show that these features are dominated Fe I with minor contributions from Fe II.

Our new spectra provide the first evidence for a sharp transition in the ejecta of SNe Ia at nebular phases. The +480 day spectrum shows a steep drop in the Fe III blend at ≈4600 Å, and the feature has disappeared by the +600 day spectrum. The adjacent spectral features at ∼4400 Å and ∼5400 Å remain strong in all of the spectra. However, these features shift and change compared to the <400 day spectra. This is likely due to the transition from Fe II to Fe I emission.

3.2. The 7300 Å Feature

The feature at ∼7300 Å is dominated by a blend of [Fe II] and [Ni II] in the nebular spectra of normal SNe Ia (e.g., Mazzali et al. 2015; Flörs et al. 2018; Maguire et al. 2018; Wilk et al. 2020). However, Figures 1, 2, and 3 show a distinct change in this feature at ≈480 days as well, with the emission profile transitioning from double to triple peaked. We consider four possible interpretations:

1. [Fe II] and [Ni II] produce the entire profile with no contribution from [Ca II];
2. [Ca II] is narrow ($<4000\,km\,s^{-1}$) and only contributes to the central peak, whereas moderate-width ($\approx8000\,km\,s^{-1}$) [Fe II] and [Ni II] produce the wings;
3. Broad [Ca II] ($\sim12{,}000\,km\,s^{-1}$) dominates the feature, with minor contributions from narrow ($\lesssim2500\,km\,s^{-1}$) [Fe II] and [Ni II] to the wings; or
4. The entire profile is produced by [Ca II] with no significant contribution from [Fe II]+[Ni II].

Case 1, where the central emission peak is attributed to [Fe II] and/or [Ni II], requires a highly asymmetric ejecta distribution that conflicts with the symmetric emission-line profiles of Co, Ni, and Fe (e.g., McClelland et al. 2013; Graham et al. 2015b). Additionally, the spherically symmetric, one-dimensional models of Fransson & Jerkstrand (2015) do not require any ejecta asymmetry to reproduce the observations. Thus, we conclude the central peak is rest-velocity [Ca II].

Case 2, where [Fe II] and [Ni II] dominate the profile with only a minor contribution from [Ca II], is plausible but we find it unlikely for several reasons. First, it requires [Ca II] to be present in the ejecta but only at low velocities ($\lesssim4000\,km\,s^{-1}$) that are typically dominated by iron-group elements (IGEs; e.g., Ruiz-Lapuente & Lucy 1992; Liu et al. 1997). Second, high-density burning can produce ^{48}Ca (Meyer et al. 1996; Domínguez & Höflich 2000), but it is likely confined to the lowest velocities ($\lesssim1000\,km\,s^{-1}$; e.g., Galbany et al. 2019), which disagrees with the observed $\approx4000\,km\,s^{-1}$ profile. Finally, ^{40}Ca is readily produced by incomplete Si burning (e.g., Thielemann et al. 1986), and Ca is observed in spectra of SN 2011fe near maximum light at $(10–25)\times10^3\,km\,s^{-1}$ (e.g., Parrent et al. 2012; Pereira et al. 2013; Zhang et al. 2016). Thus, attributing only the central component to [Ca II] would require two distinct, nonoverlapping zones within the ejecta: an outer, high-velocity zone ($v>10{,}000\,km\,s^{-1}$) responsible for

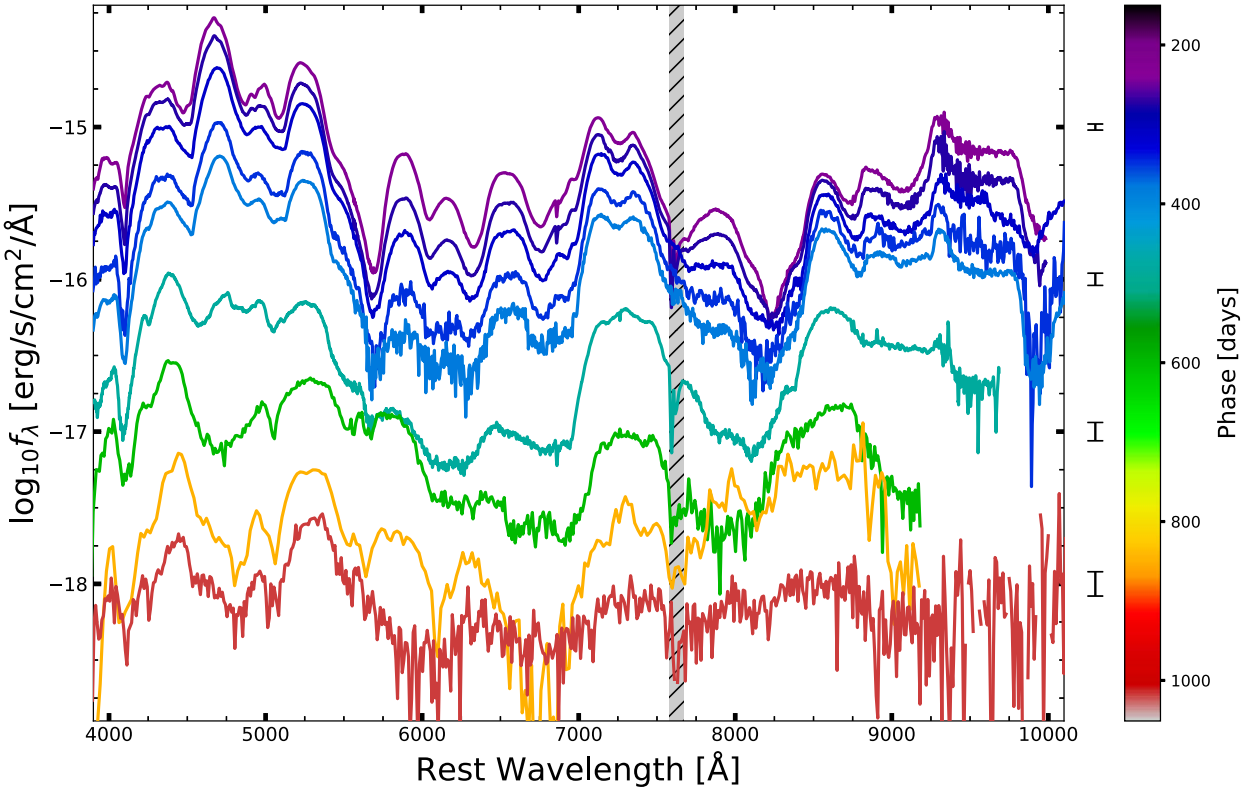

Figure 1. Flux-calibrated spectroscopic evolution of SN 2011fe at >200 days after maximum light. Error bars along the right axis represent typical flux-calibration uncertainties after the *BVR* spline fits (see Section 2). The gray hatched region marks the O_2 A-band telluric feature. The new LBT MODS spectra are provided as data behind the figure.

(The data used to create this figure are available.)

the Ca near maximum light and an inner, low-velocity zone ($v < 5000$ km s^{-1}) responsible for the nebular-phase Ca emission. This scenario is unlikely as it disagrees with the chemical stratification resulting from nuclear burning (e.g., Nomoto et al. 1984; Thielemann et al. 1986).

Case 3, where the profile is dominated by high-velocity [Ca II] with minor contributions from [Fe II] and [Ni II], is more likely considering our knowledge of chemical distribution and stratification in the ejecta (e.g., Wilk et al. 2020). This interpretation satisfies the requirement for high-velocity Ca without requiring the [Fe II] and [Ni II] contributions to disappear completely. However, attempting to model this feature with a high-velocity Ca component and Fe+Ni contributing to the wings does not provide a satisfactory fit. The residual peaks after removing a broad (≈12,000 km s^{-1}) [Ca II] component do not have a self-consistent velocity shift for the [Fe II] and [Ni II] line profiles. The blueshifted peak can be attributed to slightly blueshifted (≈−500 km s^{-1}) [Fe II], similar to <400 day spectra (e.g., McClelland et al. 2013), but it then requires redshifted [Fe II] (≈+1500 km s^{-1}) or [Ni II] (≈+3500 km s^{-1}) to explain the peak at ≈7500 Å. These mismatching velocity shifts suggest this is also an unsatisfactory explanation for the 7300 Å feature.

This leaves Case 4, where both the central peak and wing components are all created by [Ca II]. To test this idea, we show the line profile reflected about the central wavelength in Figure 4. Allowing for some ambiguities in the central wavelength because it is a blended doublet, the profiles are remarkably symmetric. More evidence for the [Ca II] interpretation comes from the lack of significant evolution between the ≈480 day spectrum and the ≈1000 day spectrum. The 4000–6000 Å region shows noticeable evolution in both line profiles and line strengths over these epochs, likely due to the dominant line emission shifting from Fe III to Fe II+Fe I (Section 3.1). We would expect some evolution at $(t - t_{max}) \gtrsim 500$ days in the 7300 Å profile if [Fe II] and [Ni II] contributed significantly to the emission profile.

Thus, we attribute the feature at ∼7300 Å to [Ca II] at ≳450 days after t_{max}. However, this requires a rapid (≲100 days) shift in the ionization state of the ejecta from ∼450–550 days after explosion and has interesting implications for the temperature and density evolution of the ejecta, as Fe III disappears at roughly the same epoch that [Ca II] appears (Section 3.1).

This spectral evolution cannot be attributed to weak features becoming visible as other features fade. Figure 5 compares the average flux of the Fe-dominated 4000–6000 Å region and the ∼7300 Å feature,[6] showing that the Fe blends evolve smoothly with time albeit with a distinct change in the decay rate at ≈550 days after t_{max}. The [Ca II] feature generally exhibits a similar decline in flux but shows strong variations, especially at ≈500–600 days after t_{max} when the Fe region changes its decline rate. This general time period agrees with the end of the nebular-phase NIR plateau discovered by Graur et al. (2020) and coincides with a change in the optical-to-NIR flux ratio (Maguire et al. 2016; Dimitriadis et al. 2017; Graur et al. 2020), all of which suggest a distinct shift in emission properties.

[6] The average flux for the ∼7300 Å region is cut off at 7500 Å to prevent the O_2 telluric band from affecting the results (e.g., Figure 3).

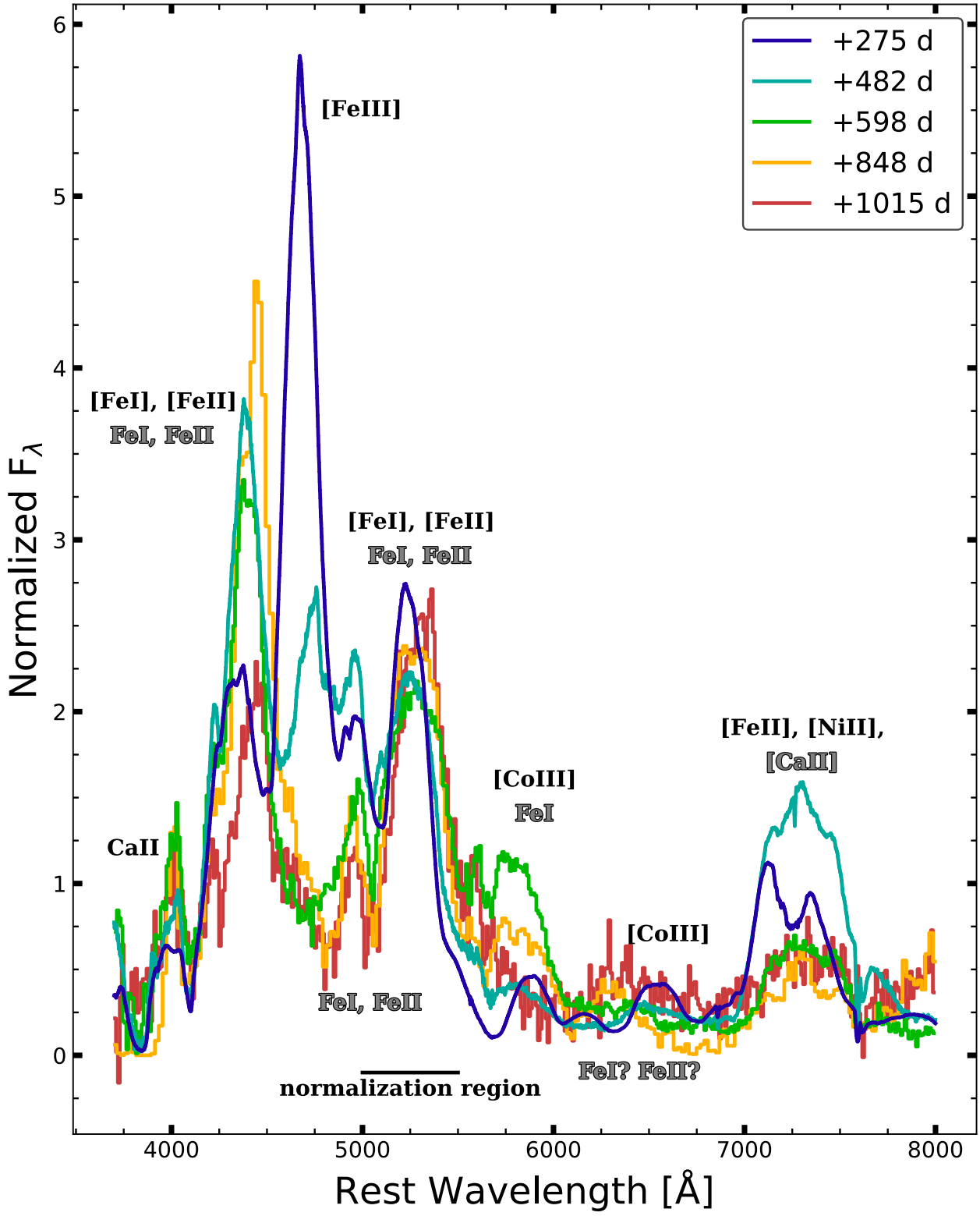

Figure 2. Spectroscopic comparison at various epochs using the same color scheme as Figure 1 but normalized by the mean flux near 5300 Å. Dominant line identifications before and after the distinct ionization transition at ∼500 days are given in black and gray, respectively. Lines with a "?" indicate that the line's contribution to the observed spectral feature is unclear. Fe emission lines after the ionization transition are likely blends of forbidden and permitted transitions (Fransson & Jerkstrand 2015), but we omit the bracket notation for visual clarity.

Interestingly, the 1000 day theoretical nebular spectra computed by Fransson & Jerkstrand (2015) using delayed-detonation (N100; Seitenzahl et al. 2013b) and pure-deflagration (W7; Iwamoto et al. 1999) explosion models both predict symmetric, triple-peaked [Ca II] profiles that qualitatively match those shown in Figure 4. However, the 1000 day model spectra are most similar to the $\leqslant$600 day observed spectra, highlighting the need for additional modeling at these epochs.

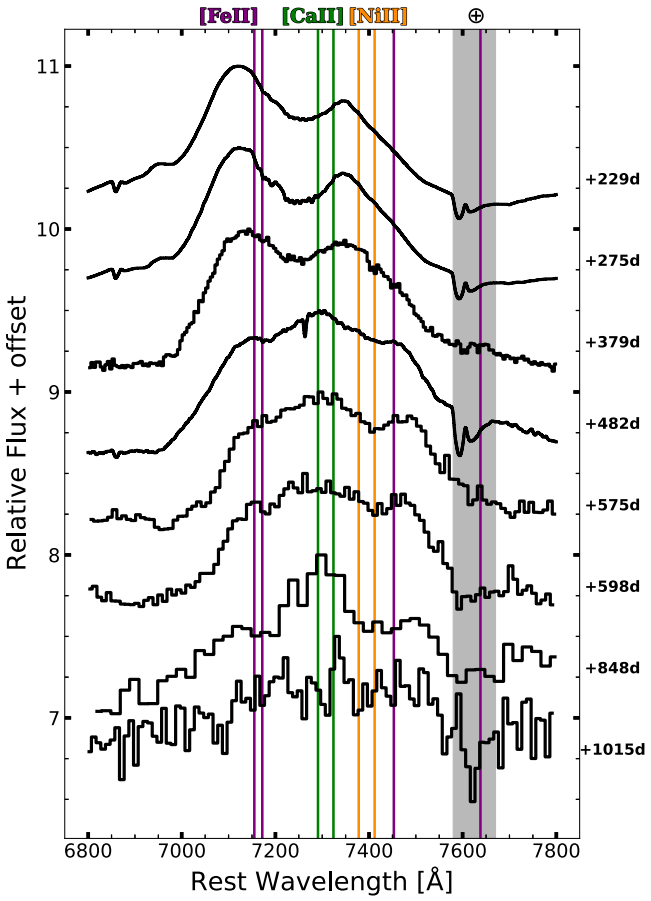

Figure 3. Temporal evolution of the 7300 Å feature, transitioning from [Fe II] +[Ni II] to [Ca II] around ∼480 days after t_{max} (see Section 3.2).

4. Progenitor System and Explosion Mechanism Constraints

The nebular spectra also provide constraints on the progenitor system of SN 2011fe. We discuss scenarios involving mass-transfer from nondegenerate companions (i.e., the "single-degenerate" scenario) in Section 4.1 and discuss double WD systems (i.e., the "double-degenerate" scenario) in 4.2.

4.1. Single-degenerate Scenarios

If a nondegenerate star was undergoing Roche-lobe overflow and depositing mass onto the WD at time of explosion, numerical simulations predict 0.1–0.5 $M_{\odot}$ of mass will be unbound from the stellar envelope (e.g., Marietta et al. 2000; Pan et al. 2012; Boehner et al. 2017), depending on the type of donor star (i.e., main-sequence versus red-giant stars). Additionally, the surrounding environment may contain H-rich material from the companion star wind or from nova-like eruptions on the WD surface during the accretion phase (e.g., Hamuy et al. 2003; Walder et al. 2008; Moore & Bildsten 2012). Signatures for such material have been searched for previously in SN 2011fe (Shappee et al. 2013; Graham et al. 2015a; Lundqvist et al. 2015), without success.

Neither H nor He are observed at any point in the spectra of SN 2011fe, and we place 10σ nondetection limits on emission lines from Hα and He Iλ5876 in the flux-calibrated spectra using Equation (3) from Tucker et al. (2020). We assume a line width of 1000 km s^{-1} that is predicted for stripped companion material

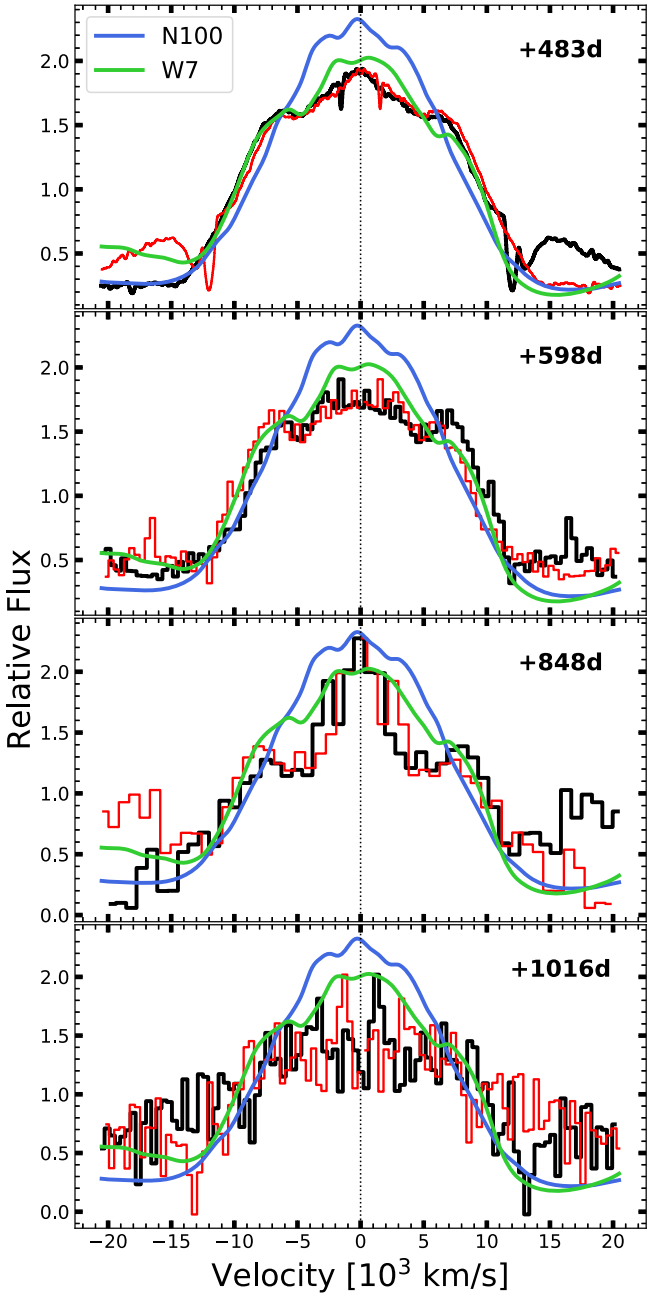

Figure 4. Velocity evolution of the continuum-subtracted [Ca II] profile at >450 days (black) compared to the theoretical 1000 day nebular spectra computed by Fransson & Jerkstrand (2015) using density profiles from the W7 deflagration model (green; Iwamoto et al. 1999) and the N100 delayed-detonation model (blue; Seitenzahl et al. 2013a). The thin red lines are the line profile reflected across the line center to highlight the profile symmetry.

(e.g., Boehner et al. 2017) and in rough agreement with emission-line widths seen in SNe Ia interacting with nearby dense circumstellar material (CSM; $v = 500$–2000 km s^{-1}; Silverman et al. 2013a, 2013b; Graham et al. 2019). The flux nondetections scale with the assumed velocity as $\propto\sqrt{v/1000\ \mathrm{km\ s^{-1}}}$. Our adopted 10$\sigma$ flux limit is conservative but corresponds to a line profile that would be visibly obvious.

Figure 6 compares the Hα nondetections, including the flux-calibration uncertainties, to the most recent models (Botyánszki et al. 2018; Dessart et al. 2020). Botyánszki et al. (2018) do not provide time-dependent line luminosities so we adopt the time

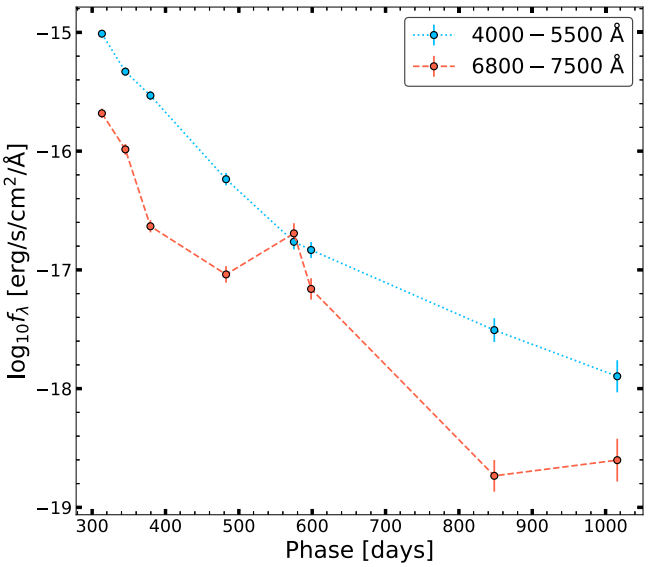

Figure 5. Evolution of the average flux for the Fe-dominated 4000–5500 Å region (dotted blue) compared to the feature at ≈7300 Å (dashed red).

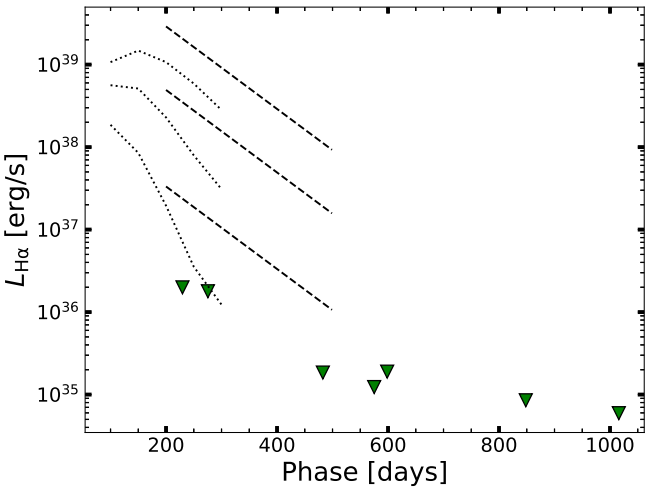

Figure 6. Nondetections of Hα (inverted triangles) compared to the models of Dessart et al. (2020, dotted lines, 100 days $\lesssim t_{\rm max} \lesssim$ 300 days) and Botyánszki et al. (2018, dashed lines, 200 days $\lesssim t_{\rm max} \lesssim$ 500 days) for ablated masses of (10^{-1}, 10^{-2}, 10^{-3}) $M_{\odot}$, from top to bottom. Flux limits for Hα, He Iλ5876, and [O I]λ6300 are provided as data behind the figure.

(The data used to create this figure are available.)

dependence derived by Tucker et al. (2020). The limit on any potential stripped/ablated companion material is $\lesssim 10^{-3}\,M_{\odot}$ for both models, essentially excluding all nondegenerate H-rich donor stars. The Hα nondetections also disfavor the presence of an H-rich CSM. Assuming a wind velocity of 10 (100) km s^{-1}, this precludes any significant CSM production by the progenitor system in the past 7000 (700) yr. The lack of CSM is also difficult to reconcile with the core-degenerate scenario (Soker et al. 2014), although this interpretation necessarily depends on the time between merger with the stellar core and explosion.

Interpreting the lack of He is more complicated. Botyánszki et al. (2018) provide a simplified He-star model that replaces the H-rich material unbound from a main-sequence (MS) star with He-rich material. This simple model provides a direct estimate of He line luminosities but fails to capture the physical conditions of a He-star envelope. The differing density profiles and surface gravities between MS and He-star envelopes will affect both the amount of unbound mass and its velocity. Additionally, the models of Dessart et al. (2020) include time-dependent opacities and predict that only the NIR He I 1.083 μm is produced at detectable levels. Thus, while we can confidently exclude any He emission at similar flux limits to those on Hα shown in Figure 6, it is not clear how to interpret this as a limit on ablated mass from a companion.

4.2. Double-degenerate Scenarios

Observational signatures of double-degenerate progenitor systems are subtle due the compact nature of both stars, but some constraints can be obtained from the nebular-phase spectra. First, we checked for [O I]λλ6300,6364 emission lines as this may indicate the violent merger of two WDs (Kromer et al. 2013) as seen in the subluminous SN Ia 2010lp (Taubenberger et al. 2013). However, both the archival and new spectra have no evidence for any O emission. This argues against a violent merger producing SN 2011fe, but the nebular-phase model parameter space for violent mergers is also largely unexplored.

Another potential double-degenerate scenario is a direct (head-on) collision, usually induced by orbital perturbations from external bodies (e.g., Thompson 2011; Antognini et al. 2014), which then produces highly asymmetric ejecta (e.g., Rosswog et al. 2009; van Rossum et al. 2016). Observationally, bimodal and asymmetric emission-line profiles of iron-group elements (IGEs) have been seen in nebular-phase SNe Ia spectra and used to infer explosion asymmetry (e.g., Dong et al. 2015; Mazzali et al. 2018; Vallely et al. 2020; Hoeflich et al. 2021). However, the Co, Fe, and [Ca II] line profiles are symmetric (see Section 3) and the one-dimensional models of Fransson & Jerkstrand (2015) do not require any asymmetry to reproduce the observations (Figure 4). Thus, we find no evidence for explosion asymmetry, which is tentative evidence against the direct-collision interpretation, in agreement with the inferred nucleosynthetic yield (Tucker et al. 2021a).

5. Discussion

Our new spectra reveal a hitherto unseen transition in the ejecta ∼500 days after explosion. This epoch also corresponds to the decades-old prediction of Axelrod (1980), who proposed that an infrared catastrophe occurs when the ejecta temperature and density are too low to populate the ∼3 eV Fe III transitions. However, Axelrod (1980) predicted that *all* emission will be shifted into the mid-IR (MIR) regime as the only remaining cooling mechanism would be by exciting fine-structure transitions.

High-energy (∼1 MeV) ^{56}Co positrons dominate the energy input at $\lesssim$1200 day explosion (e.g., Tucker et al. 2021a). Some of these positrons heat the ejecta directly but the majority of the positrons produce nonthermal excitations and ionizations (e.g., Kozma & Fransson 1992; Jerkstrand et al. 2011; Li et al. 2012; Shingles et al. 2020), either directly or via downgraded electrons. UV photons are produced upon recombination, which are transferred to optical and NIR wavelengths though multiple scatterings and fluorescence due to the optically thick forest of Fe transitions in the UV (e.g., Pinto & Eastman 2000; Jerkstrand et al. 2011; Fransson & Jerkstrand 2015). This scenario is consistent with the failure to detect SN 2011fe at <4000 Å during the nebular phase (Kerzendorf et al. 2017).

Nonlocal radiative transfer effects explain the continued presence of optical emission at these epochs (Fransson & Jerkstrand 2015), but it does not account for the observed change in emission properties at ∼500 days after explosion. The shift from Fe II+Fe III to Fe I+Fe II suggests a "recombination wave" propagating through the ^{56}Ni region (Graur et al. 2020). However, we observe the transition at ∼500 days after explosion rather than ∼600 days predicted by the models of Fransson & Jerkstrand (2015, see their Figure 1). This discrepancy may seem minor but for spherically symmetric expansion, this changes the density at the transition by a factor of ≈1.5–2, which has important ramifications for energy deposition (see Axelrod 1980).

We propose that clumping may explain this discrepancy. Clumping in the ejecta of SNe Ia has been suggested by both observational (e.g., Black et al. 2016; Mazzali et al. 2020) and theoretical (e.g., Wilk et al. 2020) studies, but confirmation is difficult. Clumping determines where energy deposition occurs as clumps will retain energy input from radioactive decays more efficiently than the lower-density regions between them. However, the higher electron density in the clumps also increases the recombination rate and lowers the average ionization state (e.g., Mazzali et al. 2020). Wilk et al. (2020) show that varying the level of clumping, parameterized as a "filling factor," has a profound impact on the observed spectra. Increased clumping diminishes the strong Fe III blend at ∼4600 Å while increasing the strength of the [Ca II] lines. Both signatures qualitatively match the spectral transition we observe ∼500 days after explosion.

However, it is unclear if these simple comparisons match the true physical evolution of the ejecta, as the interpretation of [Ca II] is also dependent on the adopted explosion model. The M_{Ch} and sub-M_{Ch} explosions models from Wilk et al. (2020) differ in Ca production by a factor of ∼2. The sub-M_{Ch} double-detonation explosion models of Polin et al. (2021) also predict nebular-phase [Ca II]. The off-center M_{Ch} delayed-detonation models of Hoeflich et al. (2021), designed to replicate a low-luminosity SN Ia, predict strong and asymmetric nebular-phase [Ca II] emission. Thus, it remains unclear which model(s) accurately predict [Ca II] emission after the nebular-phase ionization change without introducing new discrepancies with other observations of SN 2011fe.

Observationally, [Ca II] is absent in spectra of SNe Ia obtained $\lesssim$500 days after explosion (e.g., Graham et al. 2017; Flörs et al. 2018; Maguire et al. 2018; Flörs et al. 2020). However, [Ca II] is observed in the underluminous 91bg-like (e.g., SNe 1991bg, Turatto et al. 1996; 1999by, Blondin et al. 2018; 2006mr, Stritzinger et al. 2010) and 02es-like (e.g., SNe 2010lp, Taubenberger et al. 2013; 2019yvq, Siebert et al. 2020; Tucker et al. 2021b; Burke et al. 2021) subclasses of SNe Ia at $\lesssim$200 days after explosion. Considering that [Ca II] is an effective coolant and a resonant transition, it is perhaps unsurprising that the time dependence of [Ca II] emission is related to the temperature and density in the ejecta. However, the [Ca II] lines in the underluminous SNe Ia are also flat-topped and symmetric, similar to SN 2011fe (Figure 4). If [Ca II] is indeed a reliable probe of the ejecta geometry, it is interesting that the [Ca II] line profiles are so similar. However, interpreting symmetric [Ca II] emission as evidence for symmetric ejecta introduces new tensions with the complex elemental distributions seen in some SN Ia remnants (e.g., Stone et al. 2021).

SN 2011fe presented a rare opportunity to study SNe Ia physics in unprecedented detail and it remains one of the best-studied astronomical objects to date (e.g., Tucker et al. 2021a). If the sharp ionization change is related to the infrared catastrophe predicted by Axelrod (1980), this transition should produce a distinct increase in the MIR flux due to fine-structure cooling. Nebular-phase Spitzer and Herschel observations of SN 2011fe (Johansson et al. 2013, 2017) did not cover the wavelength range (20–40 μm; e.g., Fransson & Jerkstrand 2015) expected for fine-structure emission lines but the upcoming James Webb Space Telescope should provide a direct test of this theory (e.g., Ashall et al. 2021).

We thank Peter Hoeflich, Zach Claytor, Connor Auge, and Michelle Togami for useful discussions and we thank the referee for constructive feedback on the manuscript.

M.A.T. acknowledges support from the DOE CSGF through grant DE-SC0019323. C.S.K. and K.Z.S. are supported by NSF grants AST-1814440 and AST-1907570.

The LBT is an international collaboration among institutions in the United States, Italy and Germany. LBT Corporation partners are: The University of Arizona on behalf of the Arizona Board of Regents; Istituto Nazionale di Astrofisica, Italy; LBT Beteiligungsgesellschaft, Germany, representing the Max-Planck Society, The Leibniz Institute for Astrophysics Potsdam, and Heidelberg University; The Ohio State University, representing OSU, University of Notre Dame, University of Minnesota and University of Virginia.

ORCID iDs

M. A. Tucker https://orcid.org/0000-0002-2471-8442
C. Ashall https://orcid.org/0000-0002-5221-7557
B. J. Shappee https://orcid.org/0000-0003-4631-1149
C. S. Kochanek https://orcid.org/0000-0001-6017-2961
P. Garnavich https://orcid.org/0000-0003-4069-2817

References

Antognini, J. M., Shappee, B. J., Thompson, T. A., & Amaro-Seoane, P. 2014, MNRAS, 439, 1079
Ashall, C., Baron, E., Hoeflich, P. A., et al. 2021, MIR Spectroscopy of Type Ia Supernovae: The Key to Unlocking their Explosions and Element Production, JWST Proposal. Cycle, 1, 2014
Axelrod, T. S. 1980, PhD thesis, California Univ., Santa Cruz
Black, C. S., Fesen, R. A., & Parrent, J. T. 2016, MNRAS, 462, 649
Blondin, S., Dessart, L., & Hillier, D. J. 2018, MNRAS, 474, 3931
Boehner, P., Plewa, T., & Langer, N. 2017, MNRAS, 465, 2060
Botyánszki, J., & Kasen, D. 2017, ApJ, 845, 176
Botyánszki, J., Kasen, D., & Plewa, T. 2018, ApJL, 852, L6
Burke, J., Howell, D. A., Sarbadhicary, S. K., et al. 2021, ApJ, 919, 142
Dessart, L., Leonard, D. C., & Prieto, J. L. 2020, A&A, 638, A80
Dimitriadis, G., Sullivan, M., Kerzendorf, W., et al. 2017, MNRAS, 468, 3798
Domínguez, I., & Höflich, P. 2000, ApJ, 528, 854
Dong, S., Katz, B., Kushnir, D., & Prieto, J. L. 2015, MNRAS, 454, L61
Firth, R. E., Sullivan, M., Gal-Yam, A., et al. 2015, MNRAS, 446, 3895
Flörs, A., Spyromilio, J., Maguire, K., et al. 2018, A&A, 620, A200
Flörs, A., Spyromilio, J., Taubenberger, S., et al. 2020, MNRAS, 491, 2902
Fransson, C., & Jerkstrand, A. 2015, ApJL, 814, L2
Friesen, B., Baron, E., Parrent, J. T., et al. 2017, MNRAS, 467, 2392
Fukugita, M., Ichikawa, T., Gunn, J. E., et al. 1996, AJ, 111, 1748
Galbany, L., Ashall, C., Höflich, P., et al. 2019, A&A, 630, A76
Graham, M. L., Foley, R. J., Zheng, W., et al. 2015b, MNRAS, 446, 2073
Graham, M. L., Harris, C. E., Nugent, P. E., et al. 2019, ApJ, 871, 62
Graham, M. L., Kumar, S., Hosseinzadeh, G., et al. 2017, MNRAS, 472, 3437
Graham, M. L., Nugent, P. E., Sullivan, M., et al. 2015a, MNRAS, 454, 1948
Graur, O., Maguire, K., Ryan, R., et al. 2020, NatAs, 4, 188
Hamuy, M., Phillips, M. M., Suntzeff, N. B., et al. 2003, Natur, 424, 651
Hoeflich, P., Ashall, C., Bose, S., et al. 2021, ApJ, 919, 142

Hoyle, F., & Fowler, W. A. 1960, ApJ, 132, 565
Iwamoto, K., Brachwitz, F., Nomoto, K., et al. 1999, ApJS, 125, 439
Jerkstrand, A., Fransson, C., & Kozma, C. 2011, A&A, 530, A45
Johansson, J., Amanullah, R., & Goobar, A. 2013, MNRAS, 431, L43
Johansson, J., Goobar, A., Kasliwal, M. M., et al. 2017, MNRAS, 466, 3442
Kerzendorf, W. E., McCully, C., Taubenberger, S., et al. 2017, MNRAS, 472, 2534
Kerzendorf, W. E., Taubenberger, S., Seitenzahl, I. R., & Ruiter, A. J. 2014, ApJL, 796, L26
Kozma, C., & Fransson, C. 1992, ApJ, 390, 602
Kromer, M., Pakmor, R., Taubenberger, S., et al. 2013, ApJL, 778, L18
Law, N. M., Kulkarni, S. R., Dekany, R. G., et al. 2009, PASP, 121, 1395
Li, C., Hillier, D. J., & Dessart, L. 2012, MNRAS, 426, 1671
Liu, W., Jeffery, D. J., & Schultz, D. R. 1997, ApJL, 483, L107
Lundqvist, P., Nyholm, A., Taddia, F., et al. 2015, A&A, 577, A39
Maguire, K., Sim, S. A., Shingles, L., et al. 2018, MNRAS, 477, 3567
Maguire, K., Taubenberger, S., Sullivan, M., & Mazzali, P. A. 2016, MNRAS, 457, 3254
Marietta, E., Burrows, A., & Fryxell, B. 2000, ApJS, 128, 615
Mazzali, P. A., Ashall, C., Pian, E., et al. 2018, MNRAS, 476, 2905
Mazzali, P. A., Bikmaev, I., Sunyaev, R., et al. 2020, MNRAS, 494, 2809
Mazzali, P. A., Sullivan, M., Filippenko, A. V., et al. 2015, MNRAS, 450, 2631
McClelland, C. M., Garnavich, P. M., Milne, P. A., Shappee, B. J., & Pogge, R. W. 2013, ApJ, 767, 119
Meyer, B. S., Krishnan, T. D., & Clayton, D. D. 1996, ApJ, 462, 825
Moore, K., & Bildsten, L. 2012, ApJ, 761, 182
Munari, U., Henden, A., Belligoli, R., et al. 2013, NewA, 20, 30
Nomoto, K., Thielemann, F. K., & Yokoi, K. 1984, ApJ, 286, 644
Pan, K.-C., Ricker, P. M., & Taam, R. E. 2012, ApJ, 750, 151
Parrent, J. T., Howell, D. A., Friesen, B., et al. 2012, ApJL, 752, L26
Pereira, R., Thomas, R. C., Aldering, G., et al. 2013, A&A, 554, A27
Phillips, M. M. 1993, ApJL, 413, L105
Pinto, P. A., & Eastman, R. G. 2000, ApJ, 530, 757
Pogge, R. W., Atwood, B., Brewer, D. F., et al. 2010, Proc. SPIE, 7735, 77350A
Polin, A., Nugent, P., & Kasen, D. 2021, ApJ, 906, 65
Röpke, F. K., Kromer, M., Seitenzahl, I. R., et al. 2012, ApJL, 750, L19
Rosswog, S., Kasen, D., Guillochon, J., & Ramirez-Ruiz, E. 2009, ApJL, 705, L128
Ruiz-Lapuente, P., & Lucy, L. B. 1992, ApJ, 400, 127
Sand, D. J., Graham, M. L., Botyánszki, J., et al. 2018, ApJ, 863, 24
Seitenzahl, I. R., Cescutti, G., Röpke, F. K., Ruiter, A. J., & Pakmor, R. 2013a, A&A, 559, L5
Seitenzahl, I. R., Ciaraldi-Schoolmann, F., Röpke, F. K., et al. 2013b, MNRAS, 429, 1156
Shappee, B. J., & Stanek, K. Z. 2011, ApJ, 733, 124
Shappee, B. J., Stanek, K. Z., Kochanek, C. S., & Garnavich, P. M. 2017, ApJ, 841, 48
Shappee, B. J., Stanek, K. Z., Pogge, R. W., & Garnavich, P. M. 2013, ApJL, 762, L5
Shingles, L. J., Sim, S. A., Kromer, M., et al. 2020, MNRAS, 492, 2029
Siebert, M. R., Dimitriadis, G., Polin, A., & Foley, R. J. 2020, ApJL, 900, L27
Silverman, J. M., Foley, R. J., Filippenko, A. V., et al. 2012, MNRAS, 425, 1789
Silverman, J. M., Nugent, P. E., Gal-Yam, A., et al. 2013a, ApJS, 207, 3
Silverman, J. M., Nugent, P. E., Gal-Yam, A., et al. 2013b, ApJ, 772, 125
Soker, N., García-Berro, E., & Althaus, L. G. 2014, MNRAS, 437, L66
Stone, A. G., Johnson, H. T., Blondin, J. M., et al. 2021, ApJ, 923, 233
Stritzinger, M., Burns, C. R., Phillips, M. M., et al. 2010, AJ, 140, 2036
Taubenberger, S., Elias-Rosa, N., Kerzendorf, W. E., et al. 2015, MNRAS, 448, L48
Taubenberger, S., Kromer, M., Pakmor, R., et al. 2013, ApJL, 775, L43
Thielemann, F. K., Nomoto, K., & Yokoi, K. 1986, A&A, 158, 17
Thompson, T. A. 2011, ApJ, 741, 82
Tsvetkov, D. Y., Shugarov, S. Y., Volkov, I. M., et al. 2013, CoSka, 43, 94
Tucker, M. A., Ashall, C., Shappee, B. J., et al. 2021b, ApJ, 914, 50
Tucker, M. A., Shappee, B. J., Kochanek, C. S., et al. 2021a, arXiv:2111.01144
Tucker, M. A., Shappee, B. J., Vallely, P. J., et al. 2020, MNRAS, 493, 1044
Turatto, M., Benetti, S., Cappellaro, E., et al. 1996, MNRAS, 283, 1
Vallely, P. J., Tucker, M. A., Shappee, B. J., et al. 2020, MNRAS, 492, 3553
van Dokkum, P. G. 2001, PASP, 113, 1420
van Rossum, D. R., Kashyap, R., Fisher, R., et al. 2016, ApJ, 827, 128
Walder, R., Folini, D., & Shore, S. N. 2008, A&A, 484, L9
Wilk, K. D., Hillier, D. J., & Dessart, L. 2018, MNRAS, 474, 3187
Wilk, K. D., Hillier, D. J., & Dessart, L. 2020, MNRAS, 494, 2221
Zhang, K., Wang, X., Zhang, J., et al. 2016, ApJ, 820, 67